Accounting for Spatial Variations during Photopolymerization of 1,6-hexane-diol Diacrylate in the Presence of Oxygen

Alaa El Halabi | Kaveh Abdi | Anh-Duong Dieu Vo | Ardalan Ebrahimzadeh | Jasper F. van den Hoek | Luuk van der Velden | Robin X. E. Willemse | Marjolein N. van der Linden | Piet D. Iedema | Kimberley B. McAuley

Abstract

A dynamic model is proposed for photopolymerization of 1,6-hexane-diol diacrylate (HDDA) with bifunctional initiator bis-acylphosphine oxide (BAPO) in the presence of oxygen. This partial-differential-equation (PDE) model predicts time- and spatially-varying vinyl-group conversion as well as concentrations of monomer, initiator, oxygen, and seven types of radicals. Experiments to obtain diffusivities of oxygen, BAPO and HDDA are reported. Oxygen-related parameters are estimated using real-time Fourier-transform infrared (FTIR) conversion data. FTIR experiments were conducted using a range of film thicknesses ($8-17\ \mu m$), BAPO levels ($1-4\ wt\%$) and light intensities ($200-6000\ W/m^2$). The model predicts qualitative trends. Conversion predictions for runs with high intensities ($\geq 5000\ W/m^2$) and high BAPO ($4\ wt\%$) are accurate with a root-mean-squared error (RMSE) of 0.04. Larger RMSE (0.13) for runs with lower intensities and BAPO indicates that improved parameter estimates are required. Parameter estimates will be updated using in future using a model that accounts for shrinkage during polymerization.

1. Introduction

Free-radical photopolymerization has been increasing in popularity, especially in the production of films, coatings, and a variety of optical, dental, and microelectronic applications [1-3]. This article focuses on modeling the photopolymerization of the divinyl monomer 1,6-hexanediol diacrylate (HDDA), which forms a cross-linked network of polymer chains.

The HDDA photopolymerization process involves a complex set of chemical reactions, especially when a bifunctional photo-initiator such as bis-acylphosphine oxide (BAPO) is used [4]. Several mathematical models have been developed to provide insights into the photopolymerization kinetics of HDDA and other acrylate monomers [4-15]. These models have been used to study the influences of experimental factors such as film thickness, light intensity, initiator concentration and oxygen contents [4-15]. For example, Iedema et al. developed an early model to describe the photopolymerization of HDDA in an oxygen-free environment [11]. This model provided predictions of vinyl-group conversion vs. time behavior for HDDA photopolymerization experiments with different light intensities, using a simplified kinetic scheme with only one type of polymeric free radical and one type of vinyl group [11]. The most comprehensive oxygen-free kinetic model for HDDA photopolymerization accounts for initiation, propagation, branching, backbiting, cyclization, and termination reactions resulting in four different types of free-radical end groups on the polymer chains and two types of vinyl groups (i.e., vinyl groups on the HDDA monomer and pendant vinyl groups on the polymer) [4]. Abdi et al. used conversion vs. time data and weighted least squares (WLS) parameter estimation to fit 30 kinetic parameters in this model. The experiments used for parameter estimation were conducted using a range of different film thicknesses, light intensities, and initial BAPO concentrations [4, 5]. Abdi's model produces reliable predictions of vinyl-group conversions but is unable to account for oxygen presence [4].

Oxygen presents an important complication during photopolymerization processes that are in contact with air. Oxygen diffuses into the monomer/polymer mixture and reacts with initiator radicals and carbon-centered polymeric radicals to form peroxy radicals which are much less reactive, thereby inhibiting the polymerization [2, 16]. Several early models were developed to account for oxygen inhibition in photopolymerization processes [5, 12-14, 17-20]. One of the earliest was developed by Decker et al. to study oxygen inhibition during the photopolymerization of multi-acrylate systems [19]. O'Brien et al. worked on modeling oxygen effects on photopolymerization kinetics while accounting for oxygen, initiator and monomer mass-transfer effects [17]. Goodner and Bowman also accounted for simultaneous mass transfer and polymerization, using a free-volume approach to predict changes in diffusivities and rate constants as the polymerization proceeds [20]. Andrzejewska et al. developed a model to study the influence of oxygen on termination kinetics, accounting for two kinds of radicals with different propensities to diffuse and react [18]. All these models provided new insights into the influence of oxygen inhibition on photopolymerization processes; however, they relied on highly simplified reaction schemes [12, 17-20] that might result in inaccurate model predictions for new experiments.

Recently, Vo et al. proposed a more comprehensive model to describe oxygen inhibition during HDDA photopolymerization, which builds on the detailed kinetic scheme of Abdi et al. and accounts for formation and consumption of peroxy radicals [5]. Vo's model includes 5 additional parameters, on top of Abdi's 30 parameters, which she estimated using data from 8 experimental runs conducted in the presence of oxygen. Vo's model produces reliable conversion vs. time predictions for thin films (up to 12 μm) and relatively low light intensities (up to 1000 W/m^2), but underpredicts overall vinyl-group conversion in thicker films and when higher light intensities are used. Vo et al. suggested that these discrepancies in model predictions arise because their model

does not account explicitly for spatial gradients in oxygen and other species in the film as the photopolymerization progresses [5].

The influence of oxygen-induced spatial concentration gradients during photopolymerization of HDDA and other acrylate monomers has been explored by several research groups [12, 17, 20-28]. In thicker films (~100 μm), Goodner and Bowman [20] predicted that a thin layer at the top surface has lower monomer conversion due to ongoing oxygen diffusion into the film as polymerization proceeds. However, with thinner films (~10 μm), the oxygen diffuses through the entire depth of the film, impeding conversion to various extents at different depths [12]. As such, oxygen inhibition may cause polymer films to have varying mechanical properties over their thicknesses [25, 26]. The model of Iedema et al. provides reliable fits for conversion vs. time data in thin films with low oxygen levels, but overpredicts conversion in an oxygen-rich environment. Difficulties in predicting experimental data over a wider range of conditions may be due to the simplified reaction mechanism and inaccurate parameter values used in Iedema's model [12]. The aim of the current modeling research is to develop an improved model using the comprehensive reaction scheme of Vo et al. with explicit modeling of diffusion within the HDDA polymeric film [5]. A further objective is to provide new diffusivity data for oxygen, BAPO and HDDA so that improved estimates can be obtained for model parameters related to mass-transfer and oxygen inhibition. The resulting improved HDDA photopolymerization model will be helpful for selecting appropriate recipes and operating conditions to achieve high-quality rapid printing processes [5].

The remainder of the article is organized as follows. First, new experimental results and statistical analysis are discussed. Second, an updated model is proposed which relies on Vo's reaction mechanism, but explicitly accounts for oxygen, initiator, and monomer concentration gradients in the film. This updated model, which relies on an assumption of constant film thickness, uses partial

differential equations (PDEs) to describe concentrations of reacting species and functional groups, which vary with time and position in the film. Six oxygen-related and diffusion-related parameters are then estimated based on conversion versus time data from thirty-two experimental runs. The predictive ability of the model is assessed using additional data not utilized for parameter estimation. Finally, recommendations are made regarding a future model that will account for changes in density and film thickness during the photopolymerization process.

2. Experimental Data and Statistical Analysis

2.1 Measurement of the diffusion coefficient of oxygen in HDDA

Pure HDDA films with a thickness of 1.5 mm were used to determine the oxygen solubility and oxygen diffusion coefficient in HDDA monomer. The film was first exposed to a nitrogen gas flow for approximately 90 minutes so that all atmospheric oxygen was purged from the system. After 90 minutes, air was fed to the chamber where the HDDA film is located. Oxygen concentration at the bottom of the film was measured using an optical oxygen sensor in a custom-built enclosure, which is shown schematically in Fig. S1, in the Supplementary Information.

A plot of the oxygen concentration vs time is shown in Fig. 1. The data shown in Figure 1 are responses from two replicate runs. Whiskers on the error bars correspond to one standard deviation, which was computed from a pooled variance estimate. The curve shown in Figure 1 is a plot of:

$$[O_2]_{z=z_f} = H_s^{cp}\, P_{O2}\left(1 - \frac{4}{\pi}\sum_{n=odd}^{\infty}\frac{(-1)^{\frac{n-1}{2}}}{n}e^{-\frac{\left(\frac{n\pi}{2}\right)^2 D_{O2}}{z_f^2}t}\right) \qquad (1)$$

which is the analytical solution of the oxygen material balance PDE, $\frac{\partial[O_2]}{\partial t} = D_{O_2} \frac{\partial^2[O_2]}{\partial z^2}$ using the initial condition and boundary conditions provided in Table 1 [29]. The boundary condition at $z = 0$ corresponds to an assumption of equilibrium between oxygen in the air and dissolved oxygen at the film surface. The Henry's law coefficient $H_s^{cp} = 1.18 \times 10^{-7} \frac{mol}{L\,Pa}$ and the oxygen diffusion coefficient $D_{O2} = 3.48 \times 10^{-9} \frac{m^2}{s}$ were obtained from the data in Fig. 1 using least squares regression.

Table 1- Initial and boundary conditions for solving Fick's second law.

Initial Condition	Boundary Conditions
At $t = 0$ $\quad [O_2] = 0$	At $z = 0$ (i.e., at top film surface) $[O_2] = H_s^{cp}\, P_{O2}$ Where $P_{O2} = 2.128 \times 10^4\, Pa$ At $z = z_f$ (i.e., at the film bottom) $\frac{\partial[O_2]}{\partial z} = 0$

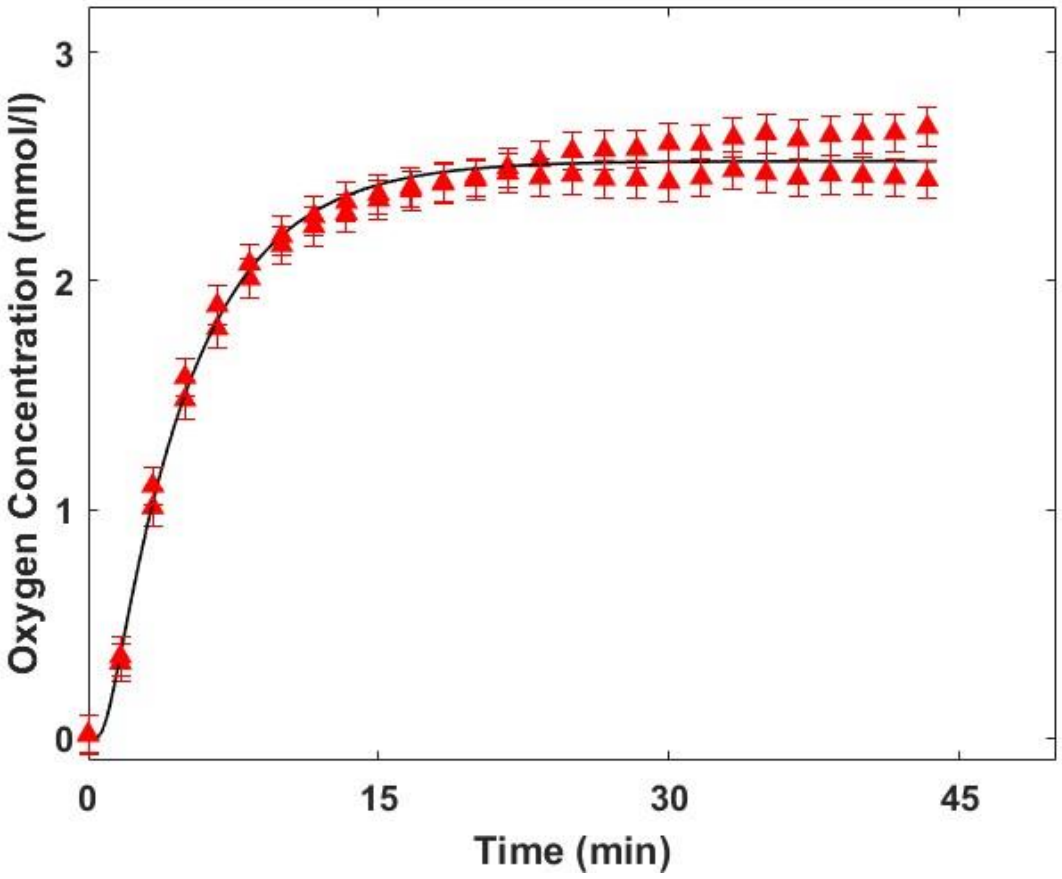

Fig. 1. Measured oxygen concentration (▲) and model predictions (—) using Equation (1)

2.2. Measurement of self diffusion coefficient for HDDA and diffusion coeffiecient of BAPO in HDDA

Diffusion coefficients of HDDA and BAPO were measured using diffusion-ordered NMR spectroscopy (DOSY). DOSY NMR works by analyzing the results of a pulsed field gradient spin echo experiment to obtain the diffusion coefficients of individual signals in a spectrum [30]. In the experimental setup, a solution containing $1\,wt\%$ BAPO was placed in a 400 MHz NMR spectrometer (magnetic field B0) and exposed to a linear magnetic field gradient ($\vec{B}$) which spatially encodes the HDDA and BAPO molecules. After a diffusion delay the molecules are

similarly decoded. The diffusion coefficient can then be calculated from the signal attenuation of each molecule. An encoding/decoding step with duration $\delta = 3000\ \mu s$ and a diffusion step with duration $\Delta = 0.2\ s$ were used to obtain NMR peaks, which resulted in calculated diffusion coefficients $D_{HDDA} = 1.59 \times 10^{-10}\ \frac{m^2}{s}$ and $D_{BAPO} = 8.78 \times 10^{-11}\ \frac{m^2}{s}$.

2.3. Measurement of overall vinyl-group conversion in HDDA polymer films

Overall vinyl-group conversion vs. time data were collected using Fourier-transform infrared reflection (FTIR) spectroscopy. The setup of the experiments used to obtain these data consists of a pure HDDA film with added BAPO initiator and Tego Rad 2250 surfactant (2 $wt\%$). These films were exposed to the air so that the initial oxygen concentration was uniform throughout. The experiments are divided into two sets. The first data set arises from 12 experimental runs that had a film thickness of ~12 μm, an initial BAPO concentration of 4 $wt\%$, and light intensities ranging from 200 W/m^2 to 6000 W/m^2. The second data set arose from an attempted factorial design involving three factors with two or three replicates for every combination, leading to 23 experimental runs. The factors film thickness (8 or 16 μm), initial BAPO concentration (1 or 4 $wt\%$), and light intensity (1000 or 5000 W/m^2). All experiments were conducted in the presence of atmospheric oxygen during polymerization. Thirty-two out of the 35 experimental runs are used for estimating the model parameters in this study, while the remaining 3 are saved for model validation. Details about the photopolymerization method and data collection are provided elsewhere [5, 12, 31]. Note that, Vo et al. used 8 out of the 35 runs for parameter estimation in their previous modelling study (i.e., runs involving thin films with relatively low light intensities). The additional 27 runs used in the current study contain new information.

3. Model Development

3.1 Reaction mechanism

The current modeling study relies on the reaction mechanism of Abdi et al. and the extension proposed by Vo et al. to account for oxygen inhibition [4, 5]. A detailed list of reactions is provided in Table S1 in the Supplementary Information. The first step in the mechanism is light-induced decomposition of one of the carbon-phosphorus bonds of the BAPO initiator (see Fig. 2). Decomposition of BAPO results in two types of radicals, a carbon-centered $I^{\bullet}$ radical and a phosphorous-centered $\tilde{I}^{\bullet}$ radical. The phosphorous-centered radical has a remaining carbon-phosphorous bond that can be decomposed in a later reaction to produce $I_P^{\bullet}$ (see Fig. 2**b**). Initiator radicals can react with vinyl groups on the HDDA monomer generating $R^{=\bullet}$. This macroradical end group $R^{=\bullet}$ has a free radical and an unreacted vinyl group (see Fig. 3**b**). We assume that the life of $R^{=\bullet}$ is too short for the vinyl groups in $R^{=\bullet}$ to be consumed by branching before the corresponding free radical reacts (assumption 4 and assumption 7 in Table S1 in the Supplementary Information).

The end group $R^{=\bullet}$ can propagate with HDDA monomer (Fig. 3**a**). When this reaction happens, the vinyl group from the $R^{=\bullet}$ whose radical is consumed becomes a pendant vinyl group V_P. End groups of type $R^{=\bullet}$ can also undergo cyclization reactions to produce the cyclic radical $C^{\bullet}$ (Fig. 3**b**). Free radical end groups such as $R^{=\bullet}$ and $C^{\bullet}$ can also participate in branching reactions by propagating with pendant vinyl groups V_P (Fig. 3**c**) to produce a branch-point radical $B^{\bullet}$. Backbiting reactions (Fig. 3**d**) produce a tertiary radical $T^{\bullet}$. In addition to these reactions, all radical species can react with oxygen to produce peroxidic radical end groups $O^{\bullet}$ (Fig. 3**e**). Peroxidic radicals undergo very slow propagation, branching and back-biting reactions. Finally,

Peroxidic radicals can terminate with other radicals in the reaction mixture. Consumption of $R^{=\bullet}$, $C^{\bullet}$, $B^{\bullet}$ and $T^{\bullet}$ radicals via termination with $O^{\bullet}$ radicals lead to an important reduction in the rate of consumption of vinyl groups.

3.2 Model equations

The proposed model accounts for spatial variation in concentrations of chemical species and end groups, leading to 13 partial differential equations (PDEs) as shown in Table 3. Equation 3.1 is a material balance on the unreacted initiator where $[I]$ is the initiator concentration in $^{mol}/_{L}$, t is the time in s, and z is the distance from the top surface of the film in m. The first term on the right-hand side accounts for initiator diffusion within the film, and the second term accounts for light-induced initiator consumption. The diffusivity D_I depends on the free volume v_f within the film, which depends on the monomer conversion X_M [12]. Algebraic equations for D_I and other variables are provided in Table 2. Notice that the second term in Equation 3.1 contains a factor of two since BAPO is a bifunctional initiator. The initiator decomposition rate constant k_d depends on light intensity I_l which decreases gradually with the film depth z (see Equations 2.1 and 2.2 in Table 2). Initial and boundary conditions for Equation 3.1 and the other PDEs in Table 3 are provided in Table S3 in the Supplementary Information.

Equations 3.2 to 3.10 are dynamic material balances on unreacted initiator fragments $\tilde{I}$, monomer M, pendant vinyl groups V_P, dissolved oxygen, and free radicals of types $R^{=\bullet}$, $C^{\bullet}$, $B^{\bullet}$, $T^{\bullet}$ and $O^{\bullet}$, respectively. Notice that the balances on monomer, initiator and oxygen contain diffusion terms, but balances on the polymeric species (i.e., $\tilde{I}$, V_p, $R^{=\bullet}$, $C^{\bullet}$, $B^{\bullet}$, $T^{\bullet}$ and $O^{\bullet}$) do not (see assumption 1 in Table S1 in the Supplementary Information). Details concerning the derivations of Equations

3.1 and 3.8 are provided in the Supplementary Information. The other PDEs in Table 3 are derived in a similar fashion.

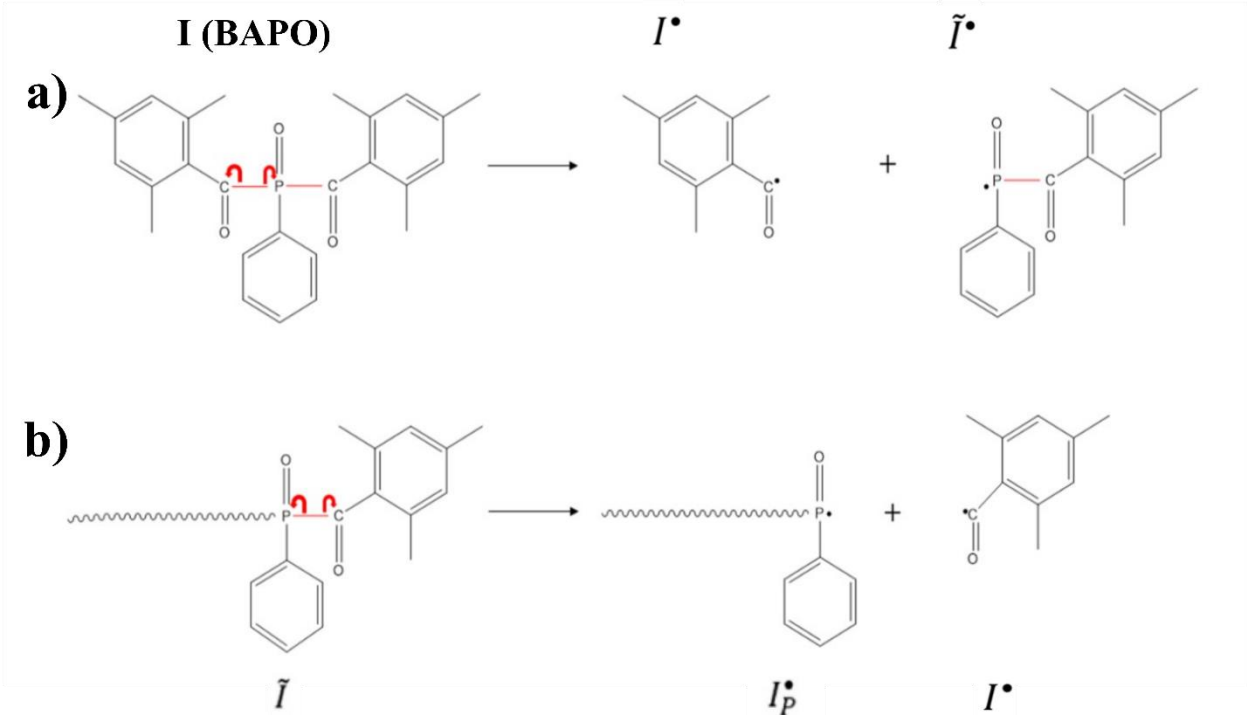

Fig. 2. Decomposition of a) initiator molecules and b) remaining carbon-phosphorous bonds in Ĩ [4, 5]

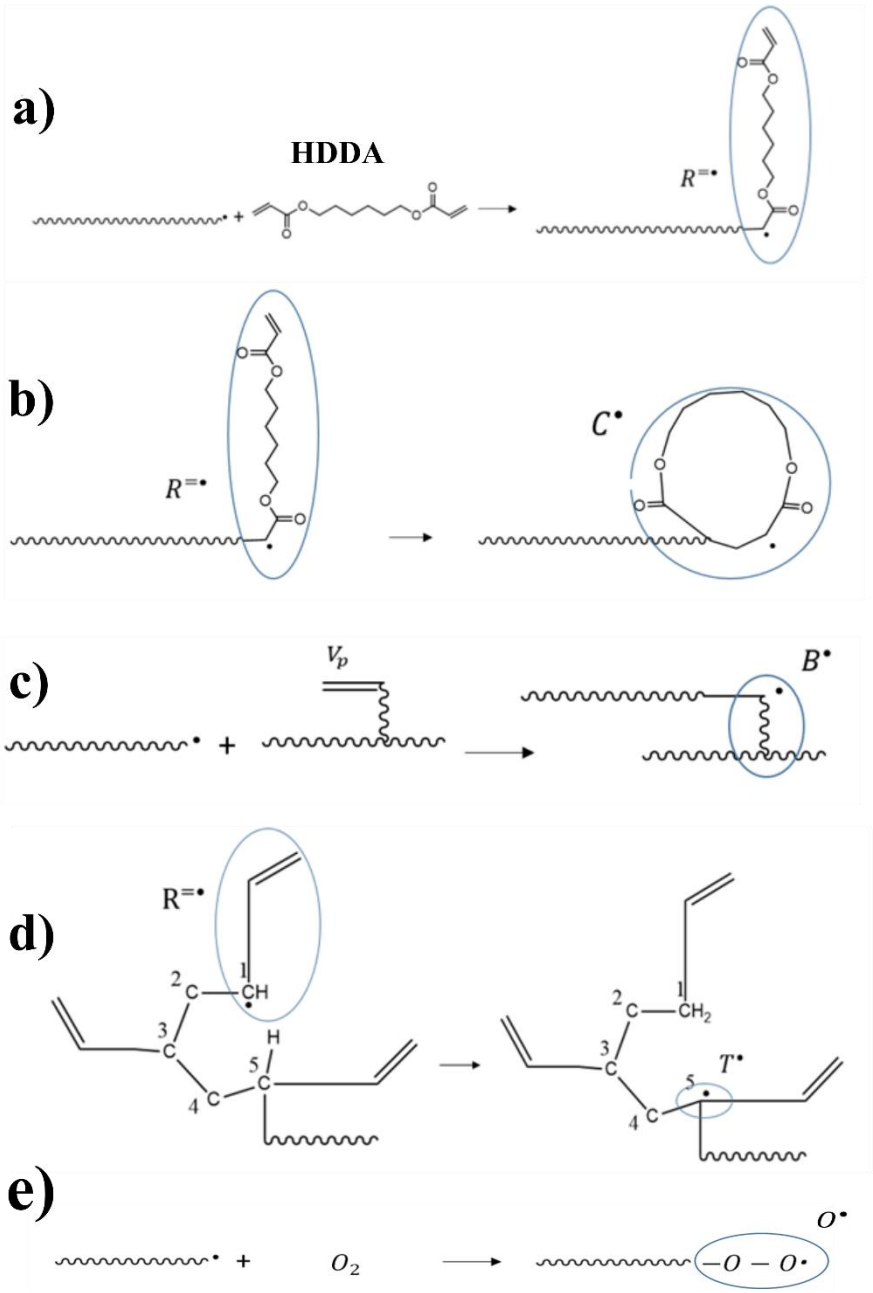

Fig. 3. Formation of different macroradicals: a) regular radical ends $R^{=\bullet}$, b) cyclized radical ends $C^{\bullet}$, c) branch-point radical ends $B^{\bullet}$, d) tertiary radical ends $T^{\bullet}$ and e) peroxidic radicals $O^{\bullet}$ [4, 5]

Table 2: List of Algebraic Equations

2.1	$I_l = I_{l,0} e^{-\varepsilon [I]_0 z}$	[20]
2.2	$k_d = \frac{\varepsilon \phi \lambda I_l}{N_A h c}$	[20]
2.3	$v_f = v_{f,0} + \left(v_{f,1} - v_{f,0}\right) X_M$	[21]
2.4	$f = 1 \Big/ \left[1 - (1 - \frac{1}{f_0}) e^{A_f \left(\frac{1}{v_f} - \frac{1}{v_{f,0}}\right)}\right]$	[6]
2.5	$k_{in,j} = k_{in,j_0} \Big/ \left[1 + e^{A_{in,j} (\frac{1}{v_f} - \frac{1}{v_{fc,in,j}})}\right]$	[32]
2.6	$k_{p,j} = k_{P,j_0} \Big/ \left[1 + e^{A_p (\frac{1}{v_f} - \frac{1}{v_{fc,p,j}})}\right]$	[32]
2.7	$k_{b,j} = k_{b,j_0} \Big/ \left[1 + e^{A_b (\frac{1}{v_f} - \frac{1}{v_{fc,b}})}\right]$	[32]
2.8	$k_C = k_{C_0} \Big/ \left[1 + e^{A_C (\frac{1}{v_f} - \frac{1}{v_{fc,c}})}\right]$	[32]
2.9	$k_{bb,j} = k_{bb,j_0} \Big/ \left[1 + e^{A_{bb} (\frac{1}{v_f} - \frac{1}{v_{fc,bb}})}\right]$	[32]
2.10	$k_{t_{in,jj}} = k_{t_{in,jj0}} \Big/ \left[1 + e^{A_{t,in,jj} (\frac{1}{v_f} - \frac{1}{v_{fc,t,jj}})}\right]$	[32]

2.11	$k_{t,ij} = \sqrt{k_{t,ii}\, k_{t,jj}}$	[33]
2.12	$k_{t,RR} = k_{t,RR_0}\left[1 + \frac{1}{e^{-A_{t,jj}\left(\frac{1}{v_f} - \frac{1}{v_{fc,t,jj}}\right)} + \frac{R_{rd} k_{p,RM}[M]}{k_{t,RR0}}}\right]^{-1}$	[21]
2.13	$D_X = D_{X\_HDDA}\, exp\left[-A_X\left(\frac{1}{v_f} - \frac{1}{v_{f0}}\right)\right]$	[5]

Table 3: PDEs based on material balances for chemical species and end-groups, including steady state hypothesis where it applies.

3.1	$\frac{\partial [I]}{\partial t} = \frac{\partial}{\partial z}\left(D_I \frac{\partial [I]}{\partial z}\right) - 2k_d[I]$
3.2	$\frac{\partial [\tilde{I}]}{\partial t} = -k_{\tilde{d}}[\tilde{I}] + 2k_{in,\tilde{I}M}[\tilde{I}^\bullet][M] + k_{in,\tilde{I}V_p}[\tilde{I}^\bullet][V_p] + k_{t,\tilde{I}R}[\tilde{I}^\bullet][R^{=\bullet}] + k_{t,\tilde{I}B}[\tilde{I}^\bullet][B^\bullet] + k_{t,\tilde{I}C}[\tilde{I}^\bullet][C^\bullet] + k_{t,\tilde{I}T}[\tilde{I}^\bullet][T^\bullet] + k_{t,\tilde{I}O}[\tilde{I}^\bullet][O^\bullet] + k_{t,I\tilde{I}}[\tilde{I}^\bullet][I^\bullet] + k_{t,\tilde{I}I}[\tilde{I}^\bullet][\tilde{I}^\bullet] + k_{t,\tilde{I}I_P}[\tilde{I}^\bullet][I_P^\bullet] + k_{O_2,\tilde{I}}[\tilde{I}^\bullet][O_2]$
3.3	$\frac{\partial [I^\bullet]}{\partial t} = 2fk_d[I] + \tilde{f}k_{\tilde{d}}[\tilde{I}] - 2k_{in,IM}[M] - k_{in,IV_P}[V_P] - k_{t,IR}[R^{=\bullet}] - k_{t,IB}[B^\bullet] - k_{t,IC}[C^\bullet] - k_{t,IT}[T^\bullet] - k_{t,IO}[O^\bullet] - k_{O_2,I}[O_2]$

which becomes, after applying SSH:

$$[I^\bullet] = \frac{2fk_d[I] + \tilde{f}k_{\tilde{d}}[\tilde{I}]}{\left(\begin{array}{c} +2k_{in,IM}[M] + k_{in,IV_P}[V_P] \\ +k_{t,IR}[R^{=\bullet}] + k_{t,IB}[B^\bullet] + k_{t,IC}[C^\bullet] + k_{t,IT}[T^\bullet] \\ +k_{t,IO}[O^\bullet] + k_{O_2,I}[O_2] \end{array}\right)}$$

3.4	$\frac{\partial [\tilde{I}^\bullet]}{\partial t} = 2fk_d[I] - 2k_{in,\tilde{I}M}[M] - k_{in,\tilde{I}V_P}[V_P] - k_{t,\tilde{I}R}[R^{=\bullet}] - k_{t,\tilde{I}B}[B^\bullet] - k_{t,\tilde{I}C}[C^\bullet] - k_{t,\tilde{I}T}[T^\bullet] - k_{t,\tilde{I}I}[I^\bullet] - k_{t,\tilde{I}O}[O^\bullet] - k_{O_2,\tilde{I}}[O_2]$

which becomes, after applying SSH:

$$[\tilde{I}^\bullet] = \frac{2fk_d[I]}{\left(\begin{array}{c} +2k_{in,\tilde{I}M}[M] + k_{in,\tilde{I}V_P}[V_P] \\ +k_{t,\tilde{I}R}[R^{=\bullet}] + k_{t,\tilde{I}B}[B^\bullet] + k_{t,\tilde{I}C}[C^\bullet] + k_{t,\tilde{I}T}[T^\bullet] + k_{t,\tilde{I}I}[I^\bullet] \\ +k_{t,\tilde{I}O}[O^\bullet] + k_{O_2,\tilde{I}}[O_2] \end{array}\right)}$$

3.5 $$\frac{\partial[I_P^{\bullet}]}{\partial t} = \tilde{f}k_{\tilde{d}}\,[\tilde{I}] - 2k_{in,I_PM}\,[M] - k_{in,I_PV_P}[V_P] - k_{t,I_PR}[R^{=\bullet}] - k_{t,I_PB}[B^{\bullet}] - k_{t,I_PC}[C^{\bullet}] - k_{t,I_PT}[T^{\bullet}] - k_{t,II_P}[I^{\bullet}] - k_{t,\tilde{I}I_P}[\tilde{I}^{\bullet}] - k_{t,I_PO}[O^{\bullet}] - k_{O_2,I_P}[O_2]$$

which becomes, after applying SSH:

$$[I_P^{\bullet}] = \frac{\tilde{f}k_{\tilde{d}}\,[\tilde{I}]}{\left(\begin{array}{c}+\,2k_{in,I_PM}\,[M]+k_{in,I_PV_P}[V_P]\\ +\,k_{t,I_PR}[R^{=\bullet}]+k_{t,I_PB}[B^{\bullet}]+k_{t,I_PC}[C^{\bullet}]+k_{t,I_PT}[T^{\bullet}]+k_{t,II_P}[I^{\bullet}]+k_{t,\tilde{I}I_P}[\tilde{I}^{\bullet}]\\ +k_{t,I_PO}[O^{\bullet}]+k_{O_2,I_P}[O_2]\end{array}\right)}$$

3.6 $$\frac{\partial[M]}{\partial t} = \frac{\partial}{\partial z}\left(D_M\frac{\partial[M]}{\partial z}\right) - 2k_{in,IM}\,[I^{\bullet}][M] - 2k_{in,\tilde{I}M}\,[\tilde{I}^{\bullet}][M] - 2k_{in,I_PM}[I_P^{\bullet}][M] - 2k_{p,R}[R^{=\bullet}][M] - 2k_{p,B}\,[B^{\bullet}][M] - 2k_{p,C}\,[C^{\bullet}][M] - 2k_{p,T}\,[T^{\bullet}][M] - 2\,k_{p,O}\,[O^{\bullet}][M]$$

3.7 $$\frac{\partial[V_P]}{\partial t} = 2k_{p,R}\,[R^{=\bullet}][M] + k_{bb,R}[R^{=\bullet}] + k_{t,RR}[R^{=\bullet}][R^{=\bullet}] + k_{t,RB}[R^{=\bullet}][B^{\bullet}] + k_{t,RC}[R^{=\bullet}][C^{\bullet}] + 2k_{t,RT}[R^{=\bullet}][T^{\bullet}] + k_{t,RO}[R^{=\bullet}][O^{\bullet}] + k_{t,IR}[I^{\bullet}][R^{=\bullet}] + k_{t,\tilde{I}R}[\tilde{I}^{\bullet}][R^{=\bullet}] + k_{t,I_PR}[I_P{}^{\bullet}][R^{=\bullet}] + k_{t,BT}[B^{\bullet}][T^{\bullet}] + k_{t,CT}[C^{\bullet}][T^{\bullet}] + k_{t,TT}[T^{\bullet}][T^{\bullet}] + k_{t,TO}[O^{\bullet}][T^{\bullet}] + k_{t,IT}[I^{\bullet}][T^{\bullet}] + k_{t,\tilde{I}T}[\tilde{I}^{\bullet}][T^{\bullet}] + k_{t,I_PT}[,I_P{}^{\bullet}][T^{\bullet}] - k_{in,IV_P}[I^{\bullet}][V_P] - k_{in,\tilde{I}V_P}[\tilde{I}^{\bullet}][V_P] - k_{in,I_PV_P}[I_P^{\bullet}][V_P] - k_{b,B}[B^{\bullet}][V_P] - k_{b,C}[C^{\bullet}][V_P] - k_{b,T}[T^{\bullet}][V_P] - k_{b,O}\,[O^{\bullet}]\big[V_p\big] + k_{O_2,R}[R^{=\bullet}][O_2]$$

3.8 $$\frac{\partial[O_2]}{\partial t} = \frac{\partial}{\partial z}\left(D_{O_2}\frac{\partial[O_2]}{\partial z}\right) - k_{O_2,R}[O_2][R^{=\bullet}] - k_{O_2,B}[O_2][B^{\bullet}] - k_{O_2,C}[O_2][C^{\bullet}] - k_{O_2,T}[O_2][T^{\bullet}] - k_{O_2,I}[O_2][I^{\bullet}] - k_{O_2,\tilde{I}}[O_2][\tilde{I}^{\bullet}] - k_{O_2,I_P}[O_2][I_P{}^{\bullet}] + \frac{1}{2}k_{t,OO}[O^{\bullet}][O^{\bullet}]$$

3.9 $$\frac{\partial[R^{=\bullet}]}{\partial t} = 2k_{in,IM}\,[I^{\bullet}][M] + 2k_{in,\tilde{I}M}\,[\tilde{I}^{\bullet}][M] + 2k_{in,I_PM}[I_P^{\bullet}][M] + 2k_{p,B}\,[B^{\bullet}][M] + 2\,k_{p,C}\,[C^{\bullet}][M] + 2k_{p,T}\,[T^{\bullet}][M] + 2\,k_{p,O}\,[O^{\bullet}][M] - k_{b,R}\,[R^{=\bullet}][V_P] - k_C[R^{=\bullet}] - k_{bb,R}[R^{=\bullet}] - k_{t,RR}[R^{=\bullet}][R^{=\bullet}] - k_{t,RB}[R^{=\bullet}][B^{\bullet}] - k_{t,RC}[R^{=\bullet}][C^{\bullet}] - k_{t,RT}[R^{=\bullet}][T^{\bullet}] - k_{t,RO}[R^{=\bullet}][O^{\bullet}] - k_{t,IR}[I^{\bullet}][R^{=\bullet}] - k_{t,\tilde{I}R}[\tilde{I}^{\bullet}][R^{=\bullet}] - k_{t,I_PR}[I_P^{\bullet}][R^{=\bullet}] - k_{O_2,R}[R^{=\bullet}][O_2]$$

3.10 $$\frac{\partial[B^{\bullet}]}{\partial t} = k_{in,IV_P}\,[I^{\bullet}][V_P] + k_{in,\tilde{I}V_P}\,[\tilde{I}^{\bullet}]\big[V_p\big] + k_{in,I_PV_P}[I_P^{\bullet}][V_P] + k_{b,R}\,[R^{=\bullet}][V_P] + k_{b,C}[C^{\bullet}][V_P] + k_{b,T}\,[T^{\bullet}][V_P] + k_{b,O}\,[O^{\bullet}]\big[V_p\big] - 2\,k_{p,B}\,[B^{\bullet}][M] - k_{t,RB}[R^{=\bullet}][B^{\bullet}] - k_{t,BB}[B^{\bullet}][B^{\bullet}] - k_{t,BC}\big[[B^{\bullet}]C^{\bullet}\big] - k_{t,BT}[B^{\bullet}][T^{\bullet}] - k_{t,BO}[B^{\bullet}][O^{\bullet}] - k_{t,IB}[I^{\bullet}][B^{\bullet}] - k_{t,\tilde{I}B}[\tilde{I}^{\bullet}][B^{\bullet}] - k_{t,I_PB}[I_P{}^{\bullet}][B^{\bullet}] - k_{O_2,B}[B^{\bullet}][O_2]$$

3.11 $$\frac{\partial[C^\bullet]}{\partial t} = k_C[R^{=\bullet}] - 2\,k_{p,C}\,[C^\bullet][M] - k_{b,C}[C^\bullet][V_P] - k_{bb,R}[C^\bullet] - k_{t,RC}[R^{=\bullet}][C^\bullet] - k_{t,BC}[B^\bullet][C^\bullet] - k_{t,CC}[C^\bullet][C^\bullet] - k_{t,CT}[C^\bullet][T^\bullet] - k_{t,CO}[C^\bullet][O^\bullet] - k_{t,IC}[I^\bullet][C^\bullet] - k_{t,\tilde{I}C}[\tilde{I}^\bullet][C^\bullet] - k_{t,I_PC}[I_P{}^\bullet][C^\bullet] - k_{O_2,C}[C^\bullet][O_2]$$

3.12 $$\frac{\partial[T^\bullet]}{\partial t} = k_{bb,R}[R^{=\bullet}] + k_{bb,R}[C^\bullet] + k_{bb,O}[O^\bullet] - 2k_{p,T}\,[T^\bullet][M] - k_{b,T}\,[T^\bullet][V_P] - k_{t,RT}[R^{=\bullet}][T^\bullet] - k_{t,BT}[B^\bullet][T^\bullet] - k_{t,CT}[C^\bullet][T^\bullet] - k_{t,TT}[T^\bullet][T^\bullet] - k_{t,TO}[T^\bullet][O^\bullet] - k_{t,IT}[I^\bullet][T^\bullet] - k_{t,\tilde{I}T}[\tilde{I}^\bullet][T^\bullet] - k_{t,I_PT}[I_P^\bullet]\,[T^\bullet] - k_{O_2,T}[T^\bullet][O_2]$$

3.13 $$\frac{\partial[O^\bullet]}{\partial t} = +\,k_{O_2,I}[I^\bullet][O_2] + k_{O_2,\tilde{I}}[\tilde{I}^\bullet][O_2] + k_{O_2,I_P}[I_P^\bullet][O_2] + k_{O_2,R}[R^{=\bullet}][O_2] + k_{O_2,B}[B^\bullet][O_2] + k_{O_2,C}[C^\bullet][O_2] + k_{O_2,T}[T^\bullet][O_2] - 2\,k_{p,O}\,[O^\bullet][M] - k_{b,O}\,[O^\bullet][V_p] - k_{bb,O}[O^\bullet] - k_{t,IO}[I^\bullet][O^\bullet] - k_{t,\tilde{I}O}[\tilde{I}^\bullet][O^\bullet] - k_{t,I_PCO}[I_P^\bullet][O^\bullet] - k_{t,RO}[R^{=\bullet}][O^\bullet] - k_{t,BO}[B^\bullet][O^\bullet] - k_{t,CO}[C^\bullet][O^\bullet] - k_{t,TO}[T^\bullet][O^\bullet] - k_{t,OO}[O^\bullet][O^\bullet]$$

4. Parameter Estimation and Simulation Results

4.1 Parameter estimation

The proposed model requires 39 parameters to simulate the photopolymerization process. Fortunately, 30 of these parameters were previously estimated by Abdi et al. using their oxygen-free model (see Table 4) [4]. Three of the 9 new parameters are diffusivities ($D_{O2-HDDA}$, $D_{BAPO-HDDA}$ and $D_{HDDA-HDDA}$) which are measured directly in the current study (see Table 5). The remaining six parameters which require estimation are free-volume parameters and oxygen-related kinetic parameters whose initial guesses are provided in Table 6. Initial guesses for $k_{O_2,R}$, $\frac{k_{p,O0}}{k_{p,R0}} = \frac{k_{b,O0}}{k_{b,R0}}$ and $\frac{k_{t,OO0}}{k_{t,RR0}}$ are values obtained from Vo's parameter estimation study [5]. They are re-estimated in the current study to account for the improved model structure and information in the new data. Upper and lower parameter bounds in Table 6 are specified to ensure that all estimated parameters are physically realistic.

The least-squares objective function used for parameter estimation is:

$$J = \sum_{i=1}^{N_{X_V}} \left(X_{V_{meas},i} - X_{V,i}\right)^2 \tag{2}$$

where $X_{V_{meas},i}$ is the i^{th} measured value of overall vinyl-group conversion, $X_{V,i}$ is the corresponding model prediction and $N_{X_V} = 1{,}655$ is the number of measured values used for parameter estimation (obtained from 32 experimental runs). Prior to conducting the parameter estimation, a formal estimability analysis was performed to confirm that all six parameters could be estimated uniquely using the available data [34, 35].

The resulting parameter estimates are shown in the fourth column in Table 6. Notice that the estimate of the initiator free-volume parameter A_{BAPO} is zero. The optimizer moved this parameter to its lower bound because accounting for the influence of conversion on initiator diffusion did not improve the model predictions. This result is not surprising because the initiator is consumed rapidly, so there is not enough time for considerable initiator diffusion to occur. As a result, the diffusivity of the initiator has little influence on the model predictions. Also notice that the estimated oxygen free-volume parameter A_{O_2} is lower than the estimated HDDA free-volume parameter A_{HDDA}. This result makes physical sense because oxygen molecules are smaller than HDDA and are less impeded by reductions in free volume as polymerization proceeds.

Table 4: List of parameters and their estimates obtained from Abdi's model [4]

Parameter	Estimate	Units	Parameter	Estimate	Units
$\boldsymbol{v_{f,0}}$	6.366×10^{-2}	-	$\frac{k_{b,R0}}{k_{p,R0}}$	10.000×10^{-1}	-
$\frac{v_{f,1}}{v_{f,0}}$	4.999×10^{-1}	-	$\frac{k_{C0}}{k_{p,R0}}$	3.347	-
$\boldsymbol{f_0}$	9.959×10^{-1}	-	$\frac{k_{bb0}}{k_{p,R0}}$	1.001×10^{-3}	-
$\boldsymbol{A_f}$	5.000×10^{-1}	-	$\frac{k_{p,B0}}{k_{p,R0}} = \frac{k_{b,B0}}{k_{b,R0}}$	4.834×10^{-2}	-
$\frac{\tilde{f}}{f}$	1.200	-	$\frac{k_{p,C0}}{k_{p,R0}} = \frac{k_{b,C0}}{k_{b,R0}}$	5.008×10^{-1}	-

$\boldsymbol{\phi}$	8.995×10^{-1}	-	$\frac{k_{p,T0}}{k_{p,R0}} = \frac{k_{b,T0}}{k_{b,R0}}$	5.027×10^{-4}	-
$\frac{k_{\bar{d}}}{k_d}$	5.724×10^{-1}	-	$k_{t_{in}II0}$	6.983×10^{8}	L $mol^{-1}s^{-1}$
$k_{in,\bar{I}M0}$	1.005×10^{6}	L mol^{-1} s^{-1}	$\frac{k_{t_{in},\bar{I}\bar{I}0}}{k_{t_{in},II0}}$	1.149	-
$\frac{k_{in,IM0}}{k_{in,\bar{I}M0}}$	5.027×10^{-3}	-	R_{rd}	7.308	L mol^{-1}
$\frac{k_{in,IVp0}}{k_{in,IM0}} = \frac{k_{in,\bar{I}Vp0}}{k_{in,\bar{I}M0}} = \frac{k_{in,IpVp0}}{k_{in,IpM0}}$	9.996×10^{-1}	-	$A_{t,RR}$	10.000×10^{-1}	-
$A_{b,R}$	5.911×10^{-1}	-	$v_{fc,tRR}$	8.553×10^{-2}	-
$\frac{A_{p,R}}{A_{b,R}}$	9.451×10^{-1}	-	$k_{t,RR0}$	1.695×10^{8}	L mol^{-1} s^{-1}
$\frac{v_{fc,bR}}{v_{fc,tRR}}$	5.292×10^{-1}	-	$\frac{k_{t,BB0}}{k_{t,RR0}}$	1.001×10^{-2}	-
$\frac{v_{fc,pR}}{v_{fc,bR}}$	8.713×10^{-1}	-	$\frac{k_{t,CC0}}{k_{t,RR0}}$	1.500	-
$k_{p,R0}$	1.001×10^{4}	L mol^{-1} s^{-1}	$\frac{k_{t,TT0}}{k_{t,RR0}}$	8.795×10^{-2}	-

Table 5: List of experimentally obtained parameters.

Parameter	Value	Unit
D_{O2}^{0}	3.463×10^{-9}	$\frac{m^2}{s}$
H_s^{cp}	1.181×10^{-1}	$\frac{mol}{L\ Pa}$
D_{HDDA}^{0}	1.59×10^{-10}	$\frac{m^2}{s}$
D_{BAPO}^{0}	8.78×10^{-11}	$\frac{m^2}{s}$

Table 6: List of estimated parameters

Parameters	Lower bound	Upper bound	Estimate	Units
A_{O_2}	0	1×10^{-1}	3.7628×10^{-2}	-
$k_{O_2,R}$	1×10^{5}	1×10^{9}	7.6828×10^{6}	L.mol^{-1} s^{-1}
$\frac{k_{p,O0}}{k_{p,R0}} = \frac{k_{b,O0}}{k_{b,R0}}$	0	2×10^{-6}	1.5405×10^{-6}	-
$\frac{k_{t,OO0}}{k_{t,RR0}}$	0	5	5.6841×10^{-5}	-
A_{HDDA}	0	5×10^{-1}	3.1437×10^{-1}	-
A_{BAPO}	0	1×10^{-1}	3.6594×10^{-2}	-

4.2 Simulation results and model assessment

Fig. 4 compares the model predictions with the experimental results for the two runs that had the best fit to the data (in green) and the worst fit to the data (in red), respectively, according to their contributions to their least-squares objective function. The best-fit simulation results in green correspond to a relatively thick film (~17 μm), a medium light intensity (~1180 W/m^2) and a high BAPO level (4 $wt\%$). The worst-fit simulation results in red are obtained for a run with similar film thickness (~20 μm) and light intensity (~1200 W/m^2), but with a low BAPO level (1 $wt\%$). Plots showing the fit to the data for several additional runs used for parameter estimation are provided in the Supplementary Information. In general, plots for runs with low BAPO (e.g. see Fig. S2) reveal that the model tends to underpredict the overall conversion when initial BAPO concentration is low. This result is not surprising because most of the kinetic parameters used in the simulations were estimated by Abdi et al., using a data set where all runs were conducted using a high BAPO concentration of 4 $wt\%$. Abdi noted that there is considerable uncertainty associated with many of his model parameters and recommended future parameter estimation studies using experiments conducted over a wider operating range. Fortunately, the runs shown in Fig. 4 confirm that the model gives reliable qualitative predictions (i.e., both the model predictions and the data are in agreement that lower BAPO levels lead to lower vinyl-group conversion). Simulation and experimental results in Fig. S3, which compare the results for two runs with different film thicknesses, confirm that thicker films tend to result in higher conversions because they experience less oxygen penetration during the runs.

Fig. 5 shows the model's predictive ability using two of the three runs saved for validation. As expected, the model predicts correctly that as light intensity increases the overall vinyl-group conversion also increases. Unfortunately, the model overpredicts the conversions in the two runs

shown in Fig. 5. Fig. S4 shows that the model slightly overpredicts the conversion for the third validation run, which has lower film thickness and lower light intensity than the runs in Fig. 5.

In general, the proposed model performs better at fitting the objective function than predictions from Vo's ODE oxygen-inhibition model (i.e., the value of the objective function in Equation (2) is 49% lower). This is not surprising, since this model uses more data to get more accurate parameter estimates and uses PDEs to better account for oxygen and monomer diffusion.

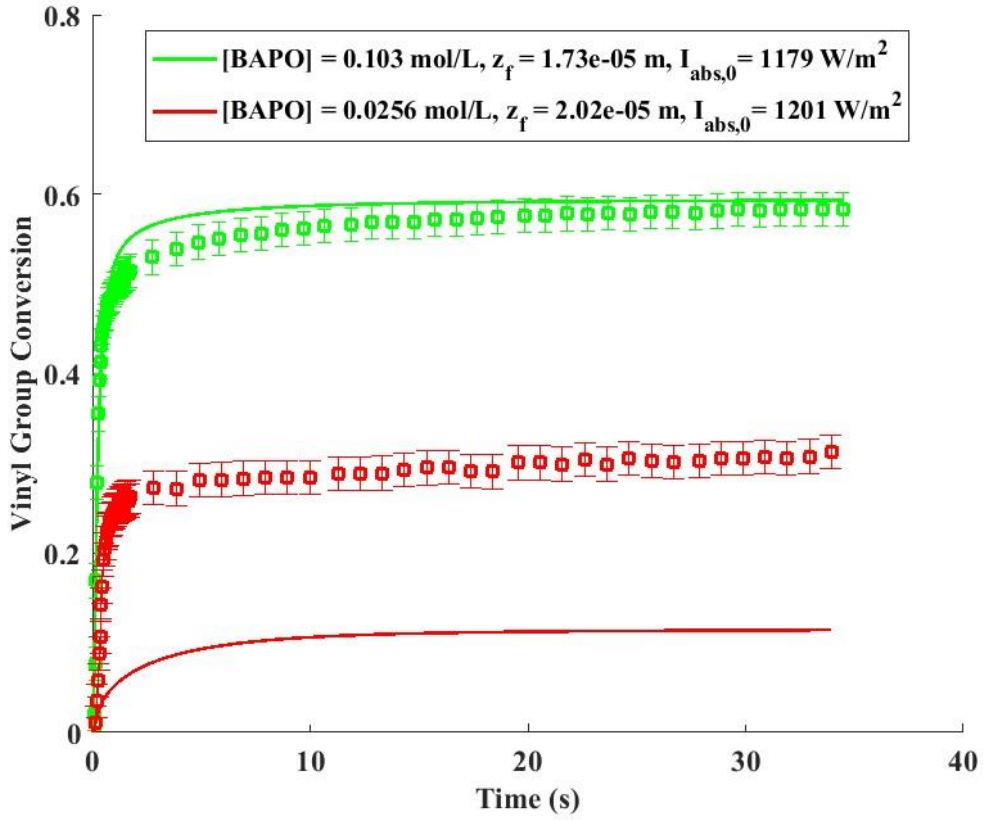

Fig. 4. Model predictions (curved lines) and the corresponding FTIR measured values for the experiments of those runs.

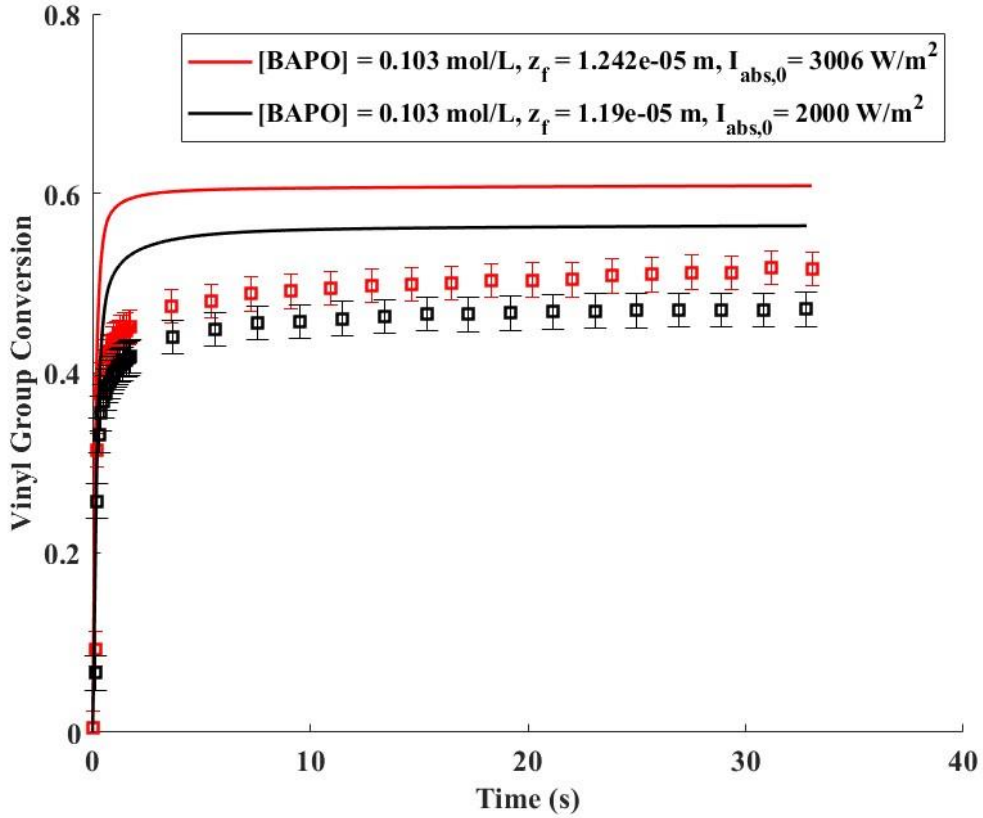

Fig. 5. Model predictions (curved lines) of the corresponding validation runs.

Fig. 6 shows predicted changes of oxygen concentrations with time at different depths in the film for a run conducted with a thick film (~18 μm), high light intensity (5916 W/m^2) and a high BAPO level (4 $wt\%$). Notice that the oxygen concentration at the top surface stays constant at $2.5 \times 10^{-3}\ mol/L$, which is in equilibrium with the air. At 10% of the film depth, the oxygen concentration drops to $\sim 1.3 \times 10^{-3}\ mol/L$ nearly instantaneously due to fast reactions with initiator radicals, and then rises slowly as the initiator concentration falls and oxygen from the air has time to diffuse into the film. At the bottom of the film the oxygen concentration remains near zero for ~0.8 s because the thick film reduces the rate of oxygen diffusion. After 3 seconds when all the reactions cease, the oxygen concentration becomes uniform within the film. Fig. 7 shows the total vinyl-group concentration changing with time at different depths within the film.

It confirms that at deeper levels within the film, the total vinyl-group concentration is lower than the concentration near the surface, because less oxygen inhibition occurs at the bottom of the film.

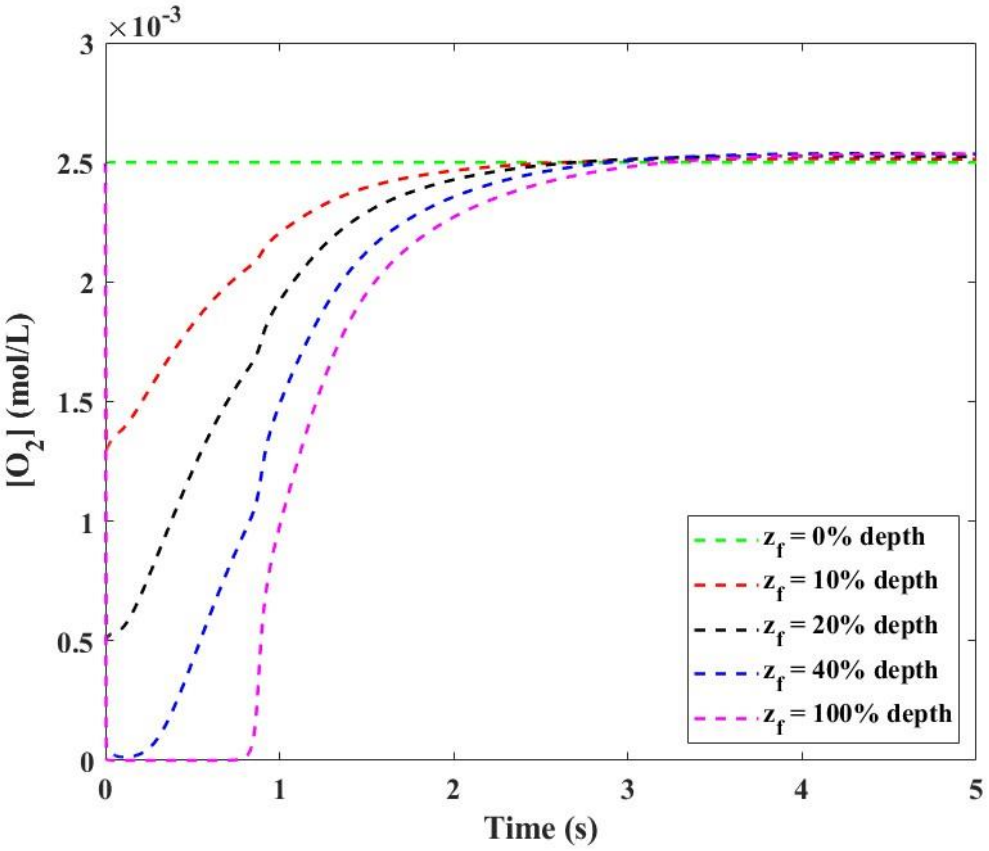

Fig. 6. Oxygen concentration levels with respect to time at different film depths

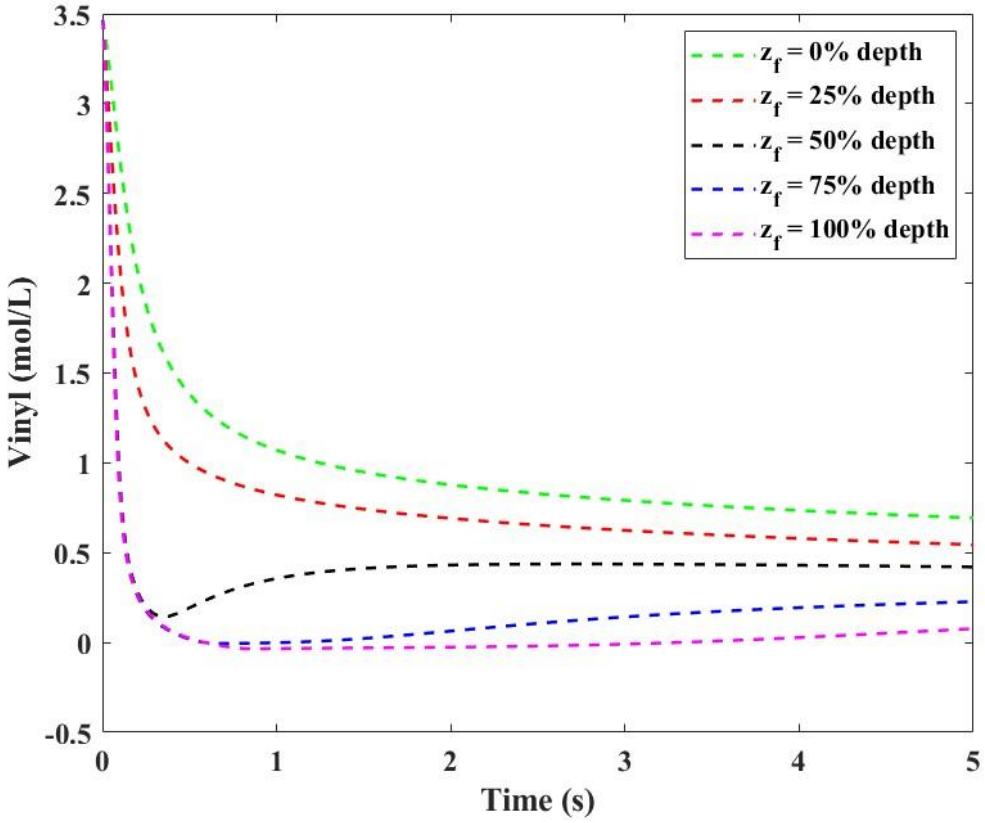

Fig. 7. Vinyl group concentration levels with respect to time at different film depths

5. Data Availability and Reproducibility Statement

The numerical data from Figures 1, 4, 5, and from Figures S2, S3 and S4 in the Supplementary Information are tabulated in an Excel spreadsheet included with the supplementary material. Error bars in Figure 1 correspond to one standard deviation which was estimated by pooling the variances for the two replicate runs in the figure. Error bars in the other figures also correspond to one standard deviation. This estimated standard deviation was obtained from replicate runs conducted at six different run conditions.

6. Conclusion

A fundamental model was developed to account for oxygen diffusion and associated inhibition during the photopolymerization of HDDA with the bifunctional initiator BAPO. This study includes experiments to measure the diffusivities of oxygen, HDDA and BAPO in HDDA. The first experiment used optical measurements to determine that $D_{O2} = 3.48 \times 10^{-9} \frac{m^2}{s}$ in HDDA monomer. The second experiment utilized DOSY NMR to determine that $D_{HDDA} = 1.59 \times 10^{-10} \frac{m^2}{s}$ and $D_{BAPO} = 8.78 \times 10^{-11} \frac{m^2}{s}$. These measured values are then used in a mathematical model that predicts concentration gradients that arise in HDDA polymer films during photopolymerization.

PDE model equations are derived based on a comprehensive reaction mechanism. Real-time FTIR data for vinyl-group conversion in 35 runs are used to support parameter estimation and model validation. The resulting PDE model and parameter estimates are used to predict the behavior of HDDA photopolymerization using a variety of film thicknesses ($8 - 17\ \mu m$), BAPO levels ($1 - 4\ wt\%$) and light intensities ($200 - 6000\ W/m^2$). The model provides accurate predictions for runs with higher BAPO levels and light intensities.

In future, it will be important to re-estimate some of the kinetic parameters obtained by Abdi et al which were held constant during the current modelling study. We are hopeful that improved parameter estimates will lead to better predictions for experiments with low BAPO levels and light intensities. The current model assumes that the film has constant density during polymerization, which is not the case. As photopolymerization proceeds, film shrinkage on the order of 10% can occur because HDDA polymer is denser than the monomer. An updated model that accounts for shrinkage is currently under development and will be used in future parameter estimation studies.

The measured diffusivities and parameter estimate from the current study will be used as initial guesses for this ongoing research, which will produce a more accurate model that can be used reliably over a wider range of conditions of industrial interest.

Acknowledgements

Financial support from MITACS is gratefully acknowledged by Anh-Duong Dieu Vo, Kaveh Abdi, and Kimberley B. McAuley. This project has received funding from the ECSEL Joint Undertaking (JU) under grant agreement No 876362. The JU receives support from the European Union's Horizon 2020 research and innovation programme and Austria, Belgium, Czech Republic, Finland, Germany, Italy, Latvia, Netherlands, Poland, and Switzerland. We thank Hennie Boonen and Jurre F. U. Tak for performing FTIR measurements.

References

[1] C. N. Bowman and C. J. Kloxin, "Toward an enhanced understanding and implementation of photopolymerization reactions," *AIChE Journal*, vol. 54, no. 11, pp. 2775-2795, 2008.

[2] E. Andrzejewska, "Photopolymerization kinetics of multifunctional monomers," *Progress in polymer science*, vol. 26, no. 4, pp. 605-665, 2001.

[3] J.-P. Fouassier, "Photoinitiation, photopolymerization, and photocuring: fundamentals and applications," *(No Title)*, 1995.

[4] K. Abdi *et al.*, "Mathematical modeling and parameter estimation for 1, 6-Hexanediol diacrylate photopolymerization with bifunctional initiator," *Chemical Engineering Science*, vol. 262, p. 118011, 2022.

[5] A. D. D. Vo *et al.*, "Mathematical modelling for 1, 6-hexanediol diacrylate photopolymerization in presence of oxygen," *The Canadian Journal of Chemical Engineering*, vol. 101, no. 9, pp. 4807-4818, 2023.

[6] M. Wenand and A. V. McCormick, "A kinetic model for radical trapping in photopolymerization of multifunctional monomers," *Macromolecules*, vol. 33, no. 25, pp. 9247-9254, 2000.

[7] J. E. Elliott, J. W. Anseth, and C. N. Bowman, "Kinetic modeling of the effect of solvent concentration on primary cyclization during polymerization of multifunctional monomers," *Chemical Engineering Science*, vol. 56, no. 10, pp. 3173-3184, 2001.

[8] D. S. Achilias and I. D. Sideridou, "Kinetics of the benzoyl peroxide/amine initiated free-radical polymerization of dental dimethacrylate monomers: experimental studies and mathematical modeling for TEGDMA and Bis-EMA," *Macromolecules*, vol. 37, no. 11, pp. 4254-4265, 2004.

[9] W. K. Neo and M. B. Chan-Park, "Application of a new model and measurement technique for dynamic shrinkage and conversion of multi-acrylates photopolymerized at different UV intensities," *Polymer*, vol. 48, no. 11, pp. 3337-3348, 2007.

[10] J. A. Gómez-Reguera, E. Vivaldo-Lima, V. A. Gabriel, and M. A. Dubé, "Modeling of the free radical copolymerization kinetics of n-butyl acrylate, methyl methacrylate and 2-ethylhexyl acrylate using PREDICI®," *Processes*, vol. 7, no. 7, p. 395, 2019.

[11] P. Iedema, V. Schamböck, H. Boonen, J. Koskamp, S. Schellekens, and R. Willemse, "Photocuring of di-acrylate," *Chemical Engineering Science,* vol. 176, pp. 491-502, 2018.

[12] P. Iedema, V. Schamböck, H. Boonen, M. van der Linden, and R. Willemse, "Photocuring of di-acrylate in presence of oxygen," *Chemical Engineering Science,* vol. 207, pp. 130-144, 2019.

[13] K. Taki, Y. Watanabe, H. Ito, and M. Ohshima, "Effect of oxygen inhibition on the kinetic constants of the UV-radical photopolymerization of diurethane dimethacrylate/photoinitiator systems," *Macromolecules,* vol. 47, no. 6, pp. 1906-1913, 2014.

[14] K. Taki, Y. Watanabe, T. Tanabe, H. Ito, and M. Ohshima, "Oxygen concentration and conversion distributions in a layer-by-layer UV-cured film used as a simplified model of a 3D UV inkjet printing system," *Chemical Engineering Science,* vol. 158, pp. 569-579, 2017.

[15] E. Limousin, E. González, D. E. Martínez-Tong, N. Ballard, and J. M. Asua, "Modelling the dynamic development of the curing process and film morphology of films cast from waterborne acrylic-alkyd hybrids," *Chemical Engineering Journal,* vol. 400, p. 125891, 2020.

[16] J. G. Kloosterboer, *Network formation by chain crosslinking photopolymerization and its applications in electronics*. Advances in Polymer Science: Springer, 1988.

[17] A. K. O'Brien and C. N. Bowman, "Modeling the effect of oxygen on photopolymerization kinetics," *Macromolecular Theory and Simulations,* vol. 15, no. 2, pp. 176-182, 2006.

[18] E. Andrzejewska, M. B. Bogacki, M. Andrzejewski, and M. Janaszczyk, "Termination mechanism during the photo-induced radical cross-linking polymerization in the presence and absence of oxygen," *Physical Chemistry Chemical Physics,* vol. 5, no. 12, pp. 2635-2642, 2003.

[19] C. Decker and A. D. Jenkins, "Kinetic approach of oxygen inhibition in ultraviolet-and laser-induced polymerizations," *Macromolecules,* vol. 18, no. 6, pp. 1241-1244, 1985.

[20] M. D. Goodner and C. N. Bowman, "Development of a comprehensive free radical photopolymerization model incorporating heat and mass transfer effects in thick films," *Chemical Engineering Science,* vol. 57, no. 5, pp. 887-900, 2002.

[21] M. D. Goodner, H. R. Lee, and C. N. Bowman, "Method for determining the kinetic parameters in diffusion-controlled free-radical homopolymerizations," *Industrial & engineering chemistry research,* vol. 36, no. 4, pp. 1247-1252, 1997.

[22] D. Panke, "Modelling the free-radical polymerization of methyl methacrylate over the complete range of conversion," *Macromolecular theory and simulations,* vol. 4, no. 4, pp. 759-772, 1995.

[23] V. V. Krongauz and E. R. Schmelzer, "Oxygen effects on anisotropic photopolymerization in polymer matrices," *Polymer,* vol. 33, no. 9, pp. 1893-1901, 1992.

[24] J. Chong, "Oxygen consumption during induction period of a photopolymerizing system," *Journal of Applied Polymer Science,* vol. 13, no. 1, pp. 241-247, 1969.

[25] M. Pilkenton, J. Lewman, and R. Chartoff, "Effect of oxygen on the crosslinking and mechanical properties of a thermoset formed by free-radical photocuring," *Journal of Applied Polymer Science,* vol. 119, no. 4, pp. 2359-2370, 2011.

[26] Z. Zhao, X. Mu, J. Wu, H. J. Qi, and D. Fang, "Effects of oxygen on interfacial strength of incremental forming of materials by photopolymerization," *Extreme Mechanics Letters,* vol. 9, pp. 108-118, 2016.

[27] J. Vrentas, J. Duda, H. C. Ling, and A. C. Hou, "Free-volume theories for self-diffusion in polymer–solvent systems. II. Predictive capabilities," *Journal of Polymer Science: Polymer Physics Edition,* vol. 23, no. 2, pp. 289-304, 1985.

[28] J. S. Vrentas and J. L. Duda, "Molecular diffusion in polymer solutions," *AIChE Journal,* vol. 25, no. 1, pp. 1-24, 1979.

[29] J. H. Lienhard IV and J. Lienhard V, H, *A heat transfer textbook*. Phlogiston Press, Cambridge 2006, p. 750.

[30] D. M. Grant and R. K. Harris, "Encyclopedia of Nuclear Magnetic Resonance, Advances in NMR," *Spectroscopy,* vol. 9, 1996.

[31] H. A. Boonen, J. A. Koskamp, W. Theiss, P. D. Iedema, and R. X. Willemse, "Simultaneous real-time analysis of bulk and bottom cure of ultraviolet-curable inks

using fourier transform infrared spectroscopy," *Applied Spectroscopy,* vol. 71, no. 12, pp. 2699-2706, 2017.

[32] K. S. Anseth and C. N. Bowman, "Reaction diffusion enhanced termination in polymerizations of multifunctional monomers," *Polymer reaction engineering,* vol. 1, no. 4, pp. 499-520, 1993.

[33] R. A. Hutchinson, "Modeling of free-radical polymerization kinetics with crosslinking for methyl methacrylate/ethylene glycol dimethacrylate," *Polymer reaction engineering,* vol. 1, no. 4, pp. 521-577, 1993.

[34] K. A. McLean and K. B. McAuley, "Mathematical modelling of chemical processes—obtaining the best model predictions and parameter estimates using identifiability and estimability procedures," *The Canadian Journal of Chemical Engineering,* vol. 90, no. 2, pp. 351-366, 2012.

[35] S. Wu, K. McAuley, and T. Harris, "Selection of simplified models: II. Development of a model selection criterion based on mean squared error," *The Canadian Journal of Chemical Engineering,* vol. 89, no. 2, pp. 325-336, 2011.